Journal of Microscopy, Vol. 191, Pt 1, July 1998, pp. 83–90.
Received 28 May 1997; accepted 4 November 1997

Quantitative and qualitative characterization of aquatic iron oxyhydroxide particles by EF-TEM

D. MAVROCORDATOS & D. PERRET
Institut de Chimie Minérale et Analytique, Université de Lausanne, BCH, CH-1015 Lausanne, Switzerland

Key words. Aquatic particles, iron (oxyhydr)oxides, goethite, energy-filtered transmission electron microscopy (EF-TEM), electron energy-loss spectroscopy (EELS), electron spectroscopic imaging (ESI), jump-ratio (JR), quantification, $L_{2,3}$ edge, $M_{2,3}$ edge, partial cross-section.

Summary

Electron energy-loss spectroscopy (EELS) and elemental imaging under the energy-filtered transmission electron microscope are powerful tools for the characterization of iron-rich particles present in natural waters. Features present in EEL spectra (Fe-$M_{2,3}$ Fe-$L_{2,3}$ and O-K ionization edges) of goethite (α-FeOOH) have been studied with an energy filter operated at 80 keV to determine optimal quantification and elemental imaging of Fe-rich natural aquatic particles in the 30–200 nm range of thickness. For quantitative aims, the Fe-$M_{2,3}$ ionization edge cannot be used easily, but the Fe-$L_{2,3}$ edge provides more accurate results owing to a better background extrapolation. The partial cross-section of the Fe(III) M shell has been determined for iron oxide. The use of two-windows (jump-ratio) and three-windows (background stripping) imaging methods is discussed in relation to the specimen thickness.

Introduction

Iron is omnipresent in lakes and rivers. Depending on the physicochemical and especially redox conditions of the ecosystem, either Fe(II) or Fe(III) can be observed as dissolved or particulate matter (Davison & De Vitre, 1992). Both species are able to play a key role in the transport of micropollutants (Salomons & Förstner, 1984; Sigg, 1985, 1987; Buffle, 1988; Buffle & van Leeuwen, 1992, 1993). Therefore, the fine characterization of iron-rich particles is a prerequisite for understanding the ultimate mechanisms involved in the scavenging processes in natural aquatic systems.

The global composition of particles within aquatic suspensions is usually determined by analytical schemes including size fractionation and conventional chemical analyses; nevertheless, the morphology, crystallinity and elemental composition of colloids at the per particle level can only be determined by analytical electron microscopy (Degueldre *et al.*, 1989; Leppard, 1992a,b). In order to retain the native morphological features of natural aquatic particles and colloids, the preparation of whole mounts by ultracentrifugation (Nomizu & Mizuike, 1986) is a fast and convenient approach; this implies that a large range of particle sizes and thicknesses (nanometres to micrometres) may be present in a single specimen.

Chemical analysis within the microscope can be obtained either by energy-dispersive spectrometry (EDS; Chandler, 1977; Reed, 1993) or by electron energy-loss spectrometry (EELS; Egerton, 1986), which are complementary (Budd & Goodhew, 1988; Robards & Wilson, 1993; Eberhart, 1995). Amongst other properties, the thickness of the specimen is one of the determining factors for the choice of the analytical method, EELS being better suited for thin specimens. Major progress has been gained in EEL spectroscopy of thin specimens studied in materials sciences, usually with post-column spectrometers operated at high voltage (100–300 keV).

For the characterization of aquatic particles (Mavrocordatos *et al.*, 1994; Perret *et al.*, 1995), we use mainly EELS on whole-mount specimens analysed at 80 keV with an on-column Castaing–Henry energy filter (EF-TEM; Castaing & Henry, 1962). The variable thickness of the particles under investigation means that special attention should be given to the interpretation of the results because of spatial inhomogeneities in multiscattering processes originating from thick regions, and because of weak signals produced by thin regions of the particles.

The aim of the present study is the optimization of the microscope and spectrometer settings for elemental mapping and quantitative analysis. Therefore, we used sections

Correspondence to: D. Perret. Tel: (+4121)6 923 923; fax: (+4121)6 923 935; e-mail didier.perret@icma.unil.ch

of resin-embedded iron oxyhydroxides (goethite, α-FeOOH) as models to satisfy limitations on thickness inhomogeneities of conventional whole mounts. Because of their needle-like shape as compared to other iron oxides (e.g. haematite α-Fe_2O_3, or magnetite Fe_3O_4), they are easily sectioned after embedding. Using these standard particles, we discuss the advantages and drawbacks of EEL spectra in the low-loss (Fe-$M_{2,3}$ edge) and inner-shell (Fe-$Le_{2,3}$ edge) regions for quantification and elemental mapping of iron-rich colloids in relation to their size.

Materials and methods

Specimen preparation

Mineral aquatic colloids are often associated with organic matter (Lienemann *et al.*, 1997; Buffle & Leppard, 1995a,b). These entities are very fragile and need a nondestructive specimen preparation scheme. Direct deposition of the suspension onto TEM grids by ultracentrifugation satisfies this aim (Nomizu & Mizuike, 1986; Perret *et al.*, 1994; Mavrocordatos & Perret, 1995), but does not allow control of the thickness of particles, which merely depends on their native state; this technique is thus not satisfactory for optimization of EELS measurements.

For this study, the model particles must have a predetermined thickness. In order to conjugate the latter condition and a representative aquatic particle, we used goethite (α-FeOOH; Schwertmann & Cornell, 1991) as a model. Dry particles were embedded in a water-soluble melamine resin (Nanoplast FB101; Bachhuber & Frösch, 1983; monomer:catalyst = 50:1). Prior to polymerization (48 h in an exsicator at 40 °C, followed by curing at 60 °C for 48 h), particles were preconcentrated in the tip of the mould by centrifugation. Sections were obtained by ultramicrotomy (MT-7 Research and Manufacturing) with a diamond knife (Standard, Microstar), in the 30–200 nm thickness range, and deposited onto TEM copper grids (200 mesh, carbon-coated, collodion-covered).

TEM and EF-TEM analysis

Specimens were first visualized and checked on a JEOL TEMSCAN 1200 EX II (LaB_6 source, 80 keV) in TEM mode. A Zeiss CEM902 EF-TEM (W source, 80 keV) with a Castaing–Henry filter was then used for spectroscopic measurements and elemental imaging. The EELS detector is a scintillator connected to a photomultiplier.

The EELS (Kontron) and Origin (Microcal) softwares were used to display and manipulate spectra (background removal, integration of features). In elemental imaging modes, a TV camera (Dage SIT 66) connected to a frame grabber allowed us to acquire digital images at various energy losses. The IBAS (Kontron) and AnalySIS (Soft-Imaging Software) softwares were used to compute and manipulate elemental maps.

Microscope and spectrometer settings

All EF-TEM analyses were processed at a beam current of *c.* 10 μA with a convergence angle $\alpha = 2{\cdot}5$ mrad (condenser aperture = 400 μm) in order to gain enough brightness for a better signal-to-noise ratio. An acceptance angle $\beta = 4$ mrad was determined by diffraction with a 47-nm-thick NiO film (Egerton & Cheng, 1994; Bennett *et al.*, 1994), corresponding to an objective aperture of 90 μm and a spectrometer entrance of 100 μm at a magnification higher than 12 000 K. For smaller magnifications, the acceptance angle β is controlled only by the objective aperture, while at higher magnifications the spectrometer aperture controls this angle. The spectrometer entrance aperture allowed us to select only the particle of interest.

The zero-loss peak ($\int I_0$) was used systematically for calibration of the energy losses (E) and absolute quantification. Relative thicknesses (t/λ, where t = thickness, λ = mean free path; for goethite, $\lambda = 93$ nm) of the sections were calculated from spectra ($\int_0^{100\,\mathrm{eV}} I_t$) according to Eq. (1) (Egerton, 1986):

$$\frac{t}{\lambda} = -\log\frac{\int I_0}{\int I_t}. \tag{1}$$

The energy resolution (δE) on the CEM-902 was selected by a slit placed under the energy filter. Different δE were tested for recording spectra and images. Ionization edges were integrated over a window (Δ) of 50 eV for absolute and relative quantification, while partial cross-sections σ were calculated according to the algorithms SigmaL2 for Fe-$L_{2,3}$ and SigmaK for O-K edges (Egerton, 1986).

Because of the lack of accurate models for M ionization edges, the partial cross-section $\sigma_{\text{Fe-M}_{2,3}}$ of the Fe-$M_{2,3}$ edge has to be determined experimentally. For this aim, we integrated the Fe-$M_{2,3}$ and the O-K edges ($I_{\mathrm{Fe}}(\beta,\Delta)$ and $I_{\mathrm{O}}(\beta,\Delta)$) after background subtraction and gain correction. The integrated Fe-$M_{2,3}$ edge was then reported versus the integrated O-K edge (Eq. (2); m = slope of the linear regression). Knowing the true atomic N_{Fe}:N_{O} ratio in goethite, the computed $\sigma_{\text{O-K}}$ and the Fe-$M_{2,3}$:O-K ratio, we were thus able to calculate the partial cross-section $\sigma_{\text{Fe-M}_{2,3}}$ for the iron $M_{2,3}$ edge, according to Eqs. (3) and (4) (Egerton, 1986):

$$\int_E^{E+\Delta} I_{\mathrm{Fe}}(\beta,\Delta) = m \times \int_E^{E+\Delta} I_{\mathrm{O}}(\beta,\Delta) \tag{2}$$

$$\frac{N_{\mathrm{Fe}}}{N_{\mathrm{O}}} = \frac{\sigma_{\mathrm{O}}(\beta,\Delta)}{\sigma_{\mathrm{Fe}}(\beta,\Delta)} \times \frac{\int_E^{E+\Delta} I_{\mathrm{Fe}}(\beta,\Delta)}{\int_E^{E+\Delta} I_{\mathrm{O}}(\beta,\Delta)} = m \times \frac{\sigma_{\mathrm{O}}(\beta,\Delta)}{\sigma_{\mathrm{Fe}}(\beta,\Delta)} \tag{3}$$

$$\sigma_{\mathrm{Fe-M}_{2,3}}(\beta,\Delta) = \sigma_{\mathrm{O-K}}(\beta,\Delta) \times m \times \frac{N_{\mathrm{O-K}}}{N_{\mathrm{Fe-M}_{2,3}}}. \tag{4}$$

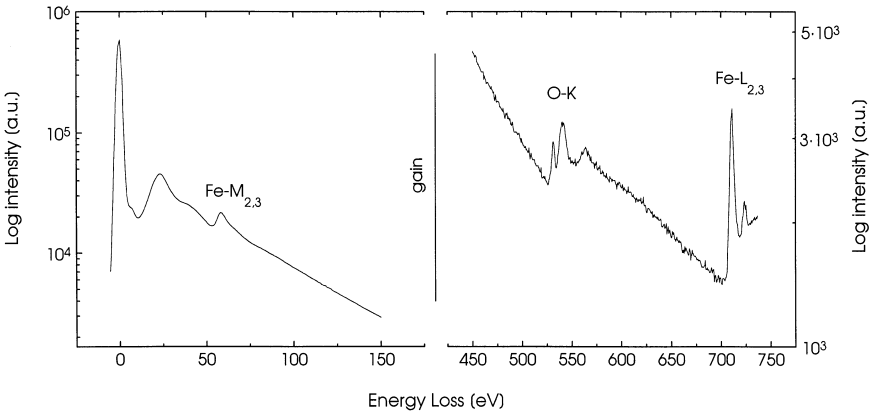

Fig. 1. Partial EEL spectrum of an ultra-thin region of a section of Nanoplast resin (*c.* 25 nm; $t/\lambda = 0{\cdot}27$) containing an individual goethite particle.

Results and discussion

Figure 1 presents the main features of the EEL spectrum obtained on an individual goethite particle within the 0–750 eV range. The different absorption edges clearly show that iron can be analysed either in the low-loss region with its $M_{2,3}$ edge or in the inner-shell region with its $L_{2,3}$ edge.

The first absorption edge in the low-loss region appears at 6·5 eV, corresponding to an Fe d–4s transition followed by an Fe 3d–4p transition at 23 eV (volume plasmon; Ditchfield, 1975). The Fe-$M_{2,3}$ edge rises at 54 eV where the background ideally follows the AE^{-r} trend in this case ($t/\lambda = 0{\cdot}27$).

Depending on the thickness of the specimen (see Fig. 2), features of the volume plasmon controlled by the Fano resonance (Egerton, 1986; Hofer & Wilhelm, 1993) influence the shape of the background above the $M_{2,3}$-edge. Therefore, extrapolation of the background becomes difficult if one uses the AE^{-r} approach; this implies that thickness effects must be taken into account if quantification or elemental mapping are required.

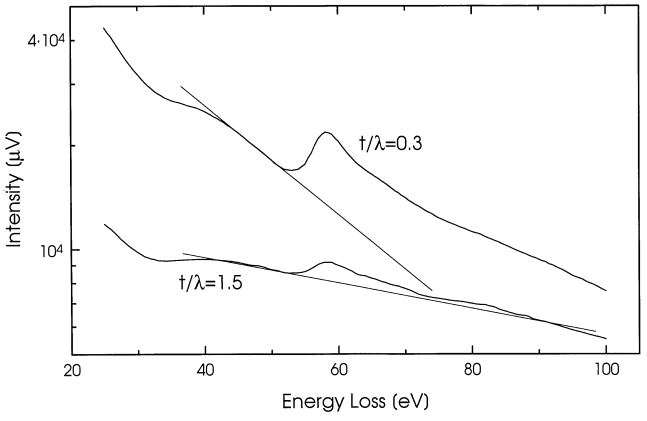

Fig. 2. Low-loss EEL spectra of thin ($t/\lambda = 0{\cdot}3$) and thick ($t/\lambda = 1{\cdot}5$) specimens of goethite, showing the difficulty of extrapolating an accurate background for thick specimens as compared to thin ones.

The typical oxygen K edge at 540 eV has been used for relative quantification. The iron $L_{2,3}$ ionization edge (Colliex, 1991) takes place at 708 eV with a transition from Fe $2p_{3/2}$ to Fe 3d (L_3 edge) followed by the transition from Fe $2p_{1/2}$ to Fe 3d (L_2 edge). These absorption edges present a drastic intensity change as compared to the background.

Figure 2 shows two spectra recorded on a thin specimen (Fig. 2a; $t/\lambda = 0{\cdot}3$) and on a thick one (Fig. 2b; $t/\lambda = 1{\cdot}5$). For thin particles, the background under the edge can be properly extrapolated using the power-law model $I = AE^{-r}$ (Hofer *et al.*, 1996). Therefore, integration of the Fe-$M_{2,3}$ absorption edge of thin specimens is possible and would allow quantification, or elemental mapping with the three-windows method. As expected, however, the thick specimen presents an important volume plasmon where the background before and under the edge obviously does not fit the AE^{-r}-equation. This implies that quantification on the Fe-$M_{2,3}$ edge becomes difficult, or even biased, when the specimen is too thick.

Quantitative approach

Figure 3a shows the absolute quantity of iron $((\int I_{Fe})/((\int I_O) \times \sigma_{Fe\text{-}L_{2,3}}))$ versus the absolute quantity of oxygen $((\int I_O)/((\int I_O) \times \sigma_{O\text{-}K}))$ obtained with spectra recorded on goethite particles of different thicknesses within the inner-shell region (O-K, Fe-$L_{2,3}$ edges). According to Eq. (3), the slope of the linear regression is the ratio Fe:O and is equal to 0·49 ± 0·01, as expected from the true atomic ratio Fe:O in goethite.

While the partial cross-section of the Fe-$M_{2,3}$ edge is now known with accuracy (Hofer & Wilhelm, 1993), and according to the fact that the O-K edge absorbs in a region requiring electronic amplification of the signal, a different treatment must be undertaken when using the Fe-$M_{2,3}$ edge. In our case, we plotted (Fig. 3b) the normalized integral of the Fe-$M_{2,3}$ edge $((\int I_{Fe})/(\int I_O))$ versus the normalized integral of the O-K edge $((\int I_O)/(\int I_O))$. Considering Eq. (4), it is thus

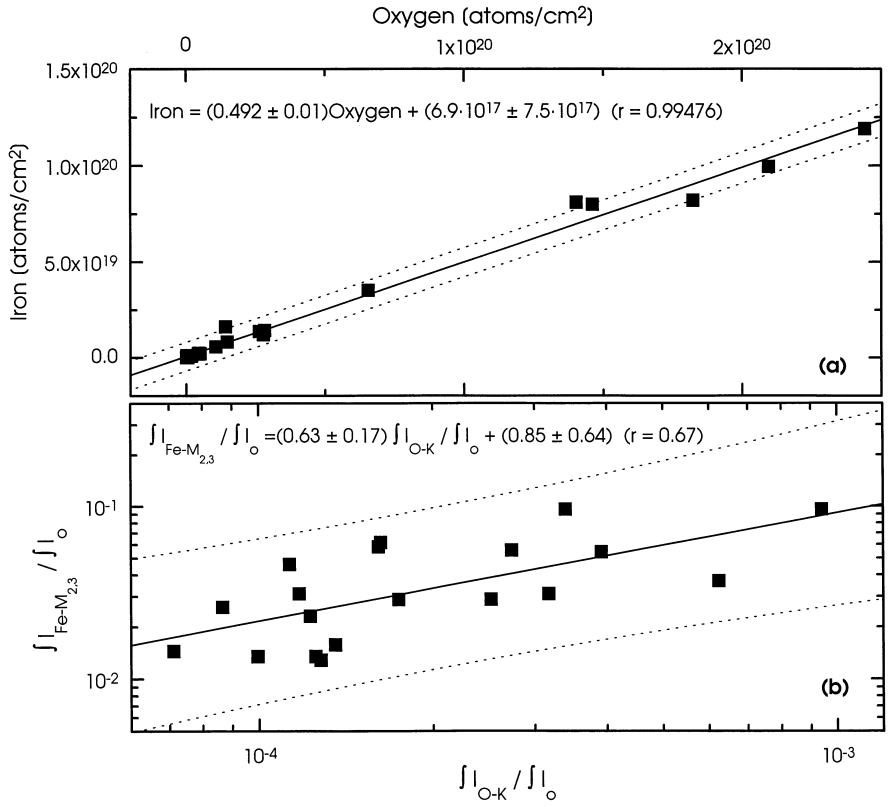

Fig 3. (a) Absolute quantification of atoms of iron $((\int I_{Fe})/((\int I_0)\times\sigma_{Fe\text{-}L_{2,3}}))$ versus atoms of oxygen $((\int I_O)/((\int I_0)\times\sigma_{O\text{-}K}))$. (b) Normalized quantification of iron $((\int I_{Fe})/(\int I_0))$ versus oxygen $((\int I_O)/(\int I_0))$. Dotted lines depict confidence bands (95%) on the linear regression.

possible to extract the partial cross-section $\sigma_{Fe\text{-}M_{2,3}}$ from the slope of the curve. In our case, the value of $\sigma_{Fe\text{-}M_{2,3}}$ is equal to $1{\cdot}48\times10^{-19}\pm2{\cdot}8\times10^{-20}$, which is in good agreement with data obtained by Hofer & Wilhelm (1993) under different working conditions $\sigma_{Fe\text{-}M_{2,3}} = 0{\cdot}993\times10^{-19}$, obtained with α-Fe_2O_3; $E_0 = 200$ keV, $\beta = 7{\cdot}6$ mrad, $\Delta = 30$ eV).

Clearly, it appears from these results that the relative quantification of the Fe:O ratio with particles of different thicknesses is much more accurate with the Fe-$L_{2,3}$ edge than with the Fe-$M_{2,3}$ edge. As presented in Fig. 2, deviations are explained by a biased background extrapolation which gives rise to large uncertainties in the integration of the iron $M_{2,3}$ edge.

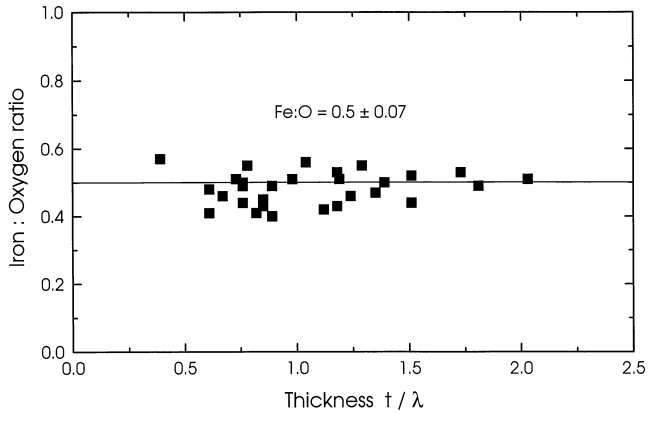

Fig. 4. Fe:O atomic ratio in goethite obtained for section thicknesses in the 20–200 nm range; the ratio was obtained using the Fe-$L_{2,3}$ and the O-K absorption edges.

Figure 4 shows the variation of the calculated elemental ratio Fe:O as a function of the relative thickness t/λ of specimens containing goethite. The ratio was measured with the Fe-$L_{2,3}$ and O-K edges, over a range of thicknesses between $t/\lambda = 0{\cdot}2$ and $t/\lambda = 2$ (average thickness of goethite particles ranging from *c.* 20 nm to *c.* 200 nm).

Our results may be compared to similar experiments reported in the literature for homogeneous boron nitride films and for nonideal specimens of polystyrene-embedded iron particles. In the case of boron nitride (Zaluzec, 1983), a deviation of the B:N ratio from ideality was already observed when film thickness increased above $t/\lambda > 1$ (*c.* 100 nm at 100 keV). However, the variability of data for thinner specimens, due to errors in the estimation of the partial cross-sections (hydrogenic model) of boron K and nitrogen K edges, was found to be below 5%. For the iron-rich polystyrene beads (Door *et al.*, 1991), the observed error on the absolute quantity of iron rose to 20% for relative thicknesses ranging from 0·2 to 0·9.

With our results, the Fe:O ratio in goethite appears to be constant over the whole range of measured thicknesses (*c.* 20–200 nm), with a variability of 14%. The deviation of the

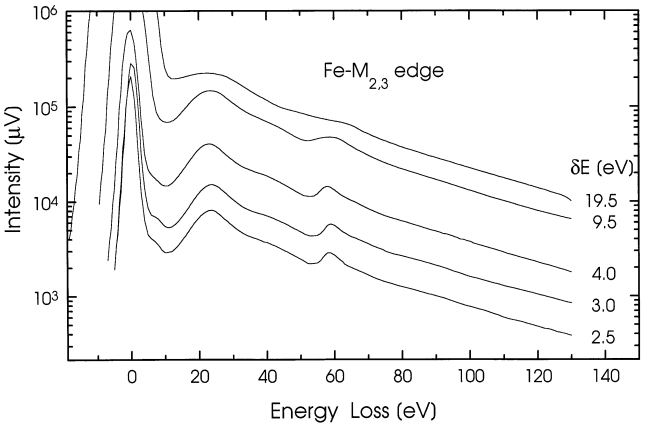

Fig. 5. EEL spectra obtained at spectrometer resolutions δE ranging from 2 eV to 20 eV for a section ($t/\lambda = 0{\cdot}7$) containing goethite particles embedded in Nanoplast resin.

linearity for thick specimens ($t/\lambda > 1$) is not observed as for boron nitride films; however, as in the case of Fe-polystyrene beads, a deviation of our results may exist, but it is probably obscured by the variability of individual data.

Qualitative approach

In practice, the Fe-$M_{2,3}$ edge is convenient to use because of the high value of its cross-section and it requires no electronic gain, as compared to edges present in the inner-shell region, which are much less intense. This edge would thus be more appropriate for elemental mapping than for quantitative work, taking into account the energy resolution used for imaging and the thickness of the specimen, which influences the shape of the spectrum in the low-loss region. The iron $M_{2,3}$ edge appears as a saw-tooth peak. Because of its shape, the signal is highly affected by the selected energy resolution δE. Figure 5 is a superimposition of spectra recorded on a single goethite particle ($t/\lambda = 0{\cdot}7$) at different values of δE. An attenuation of the Fe-$M_{2,3}$ signal is observed with a decrease of the energy resolution. At $\delta E = 4$ eV, the signal is a well-defined peak but when using a larger slit (> 10 eV), the $M_{2,3}$ edge becomes difficult if not impossible to distinguish from the background.

For elemental mapping, either the jump-ratio (JR; Johnson, 1979; Egerton & Sevely, 1983) or the background extrapolation (electron spectroscopic imaging, ESI; Egerton, 1986) approaches may be applied. In the former case, the image recorded at the absorption peak is divided by an image recorded just before the edge. In the latter case, three images are recorded: two images before the edge and one at the peak; the two first images are used for background extrapolation at the absorption peak according to AE^{-r}; this resulting image is subtracted from the image recorded at the peak. It must be emphasized that JR images do not systematically represent true elemental maps, but are a convenient alternative to ESI images when background extrapolation becomes difficult.

Figure 6 presents elemental maps of iron recorded on thin ($t/\lambda = 0{\cdot}4$; Fig. 6a–e) and thick ($t/\lambda = 1{\cdot}3$; Fig. 6f–j) specimens. In each case the JR and ESI methods were applied on the Fe-$M_{2,3}$ and Fe-$L_{2,3}$ absorption edges with the same microscope settings. In addition, we measured the signal-to-background ratio ($S/\sqrt{B}$; Hofer *et al.*, 1996) of images in order to appreciate semiquantitatively the effect of the imaging method on the resulting images (Table 1). As expected from the shape of absorption edges on EEL spectra (see Fig. 5), an energy resolution of 4 eV produced optimal results in the Fe-$M_{2,3}$ region; this avoided both saturation of the camera and signal smoothing.

Considering the results on the Fe-$M_{2,3}$ absorption edge (see Quantitative Approach), the JR method is not suited for thin specimens of goethite particles (Fig. 6b) because the signal-to-background ratio is too weak to produce sharp images. However, ESI mapping of thin specimens (Fig. 6c) gives rise to contrasted and more detailed elemental images.

On the other hand, ESI of the Fe-$M_{2,3}$ edge becomes erroneous for thick specimens (Fig. 6h) because background extrapolation cannot be calculated properly. Therefore the latter image does not contain accurate quantitative information (see Fig. 2), which results in a biased elemental map. This artefact can be avoided by using the JR procedure (Fig. 6g) because the pre-edge image is recorded at a lower intensity than the image at the absorption peak, without requiring background extrapolation. For intermediate thicknesses ($0{\cdot}5 < t/\lambda < 1$), both methods give similar results.

Owing to a better background extrapolation and a sharper peak, the Fe-$L_{2,3}$ absorption edge allows recording of JR (Figs. 6d and 6i) and ESI (Figs. 6e and 6j) images as well, for both thin and thick specimens. In the region of the Fe-$L_{2,3}$ edge, an energy resolution of 9 eV was chosen for recording images to minimize electronic gain and maximize the iron signal without noticeable smoothing of the peak.

Table 1 summarizes the signal-to-background ratios measured on the elemental maps obtained by JR and ESI, and reflects our results.

The use of the Fe-$M_{2,3}$ absorption edge represents an alternative of choice for visualizing aims: for thin specimens, ESI-$M_{2,3}$ ($S/\sqrt{B} = 18$) is more appropriate than JR-$M_{2,3}$ ($S/\sqrt{B} = 11$); ESI-$M_{2,3}$ produces images with morphological information similar to that of JR-$L_{2,3}$ ($S/\sqrt{B} = 46$) or ESI-$L_{2,3}$ ($S/\sqrt{B} = 22$). For thick specimens, either the JR-$M_{2,3}$ ($S/\sqrt{B} = 22$) or the Fe-$L_{2,3}$ JR-$L_{2,3}$ ($S/\sqrt{B} = 29$) approaches give rise to similar information. Although values of signal-to-background ratios provide semiquantitative information on the quality of the images, they are not representative of the morphological details of the particles, which can only be determined by visual inspection of the elemental maps.

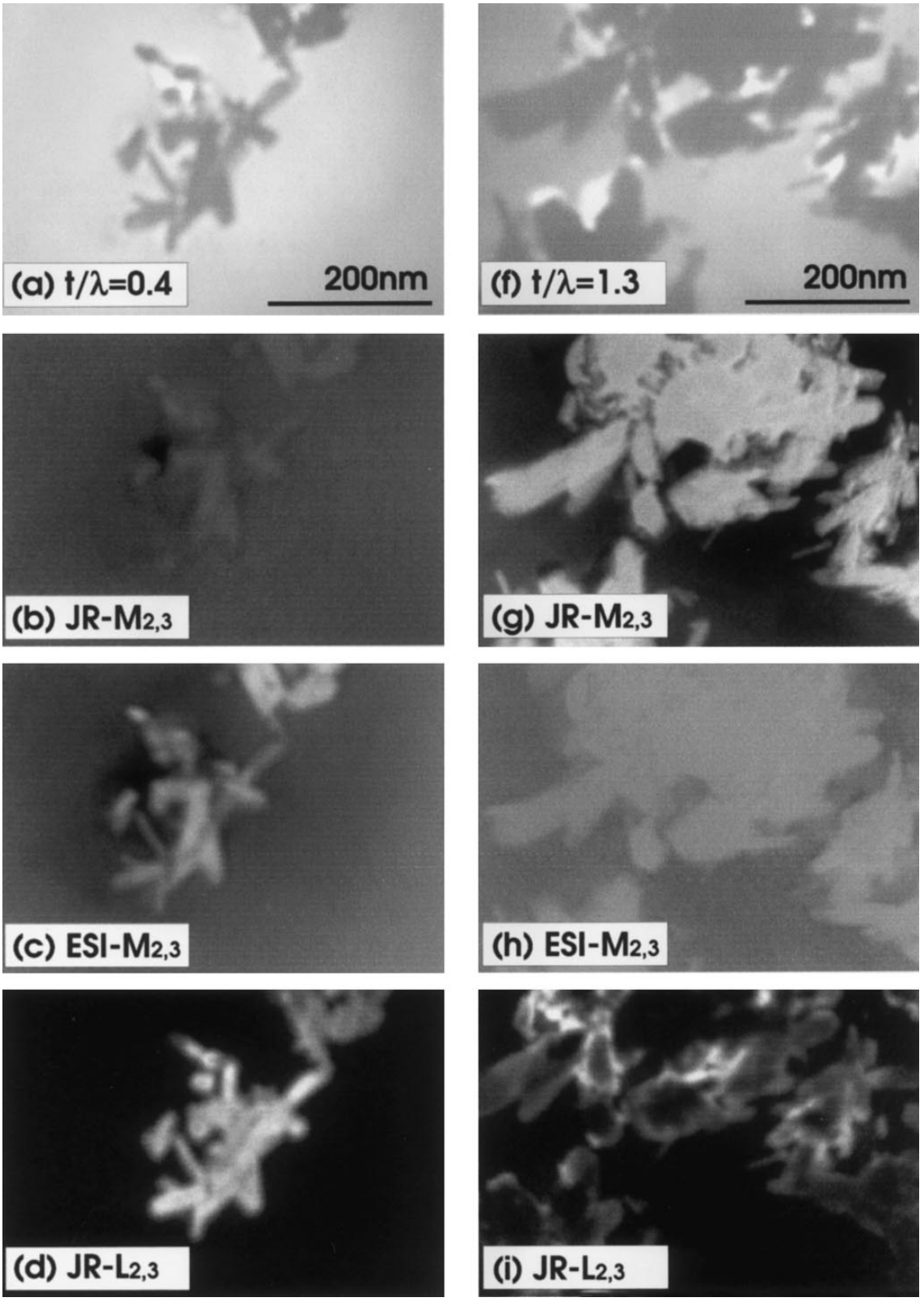
(a) t/λ=0.4
200nm
(f) t/λ=1.3
200nm
(b) JR-M2,3
(g) JR-M2,3
(c) ESI-M2,3
(h) ESI-M2,3
(d) JR-L2,3
(i) JR-L2,3

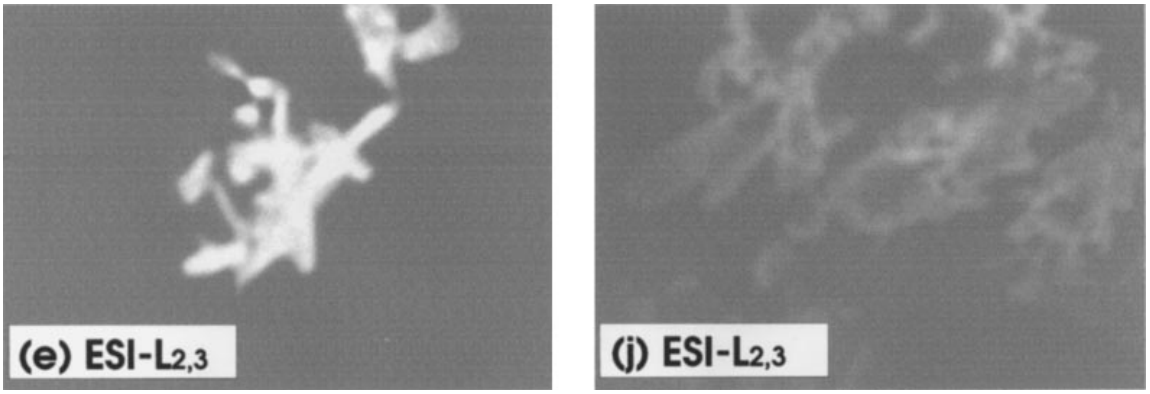

Fig. 6. Bright-field TEM (a,f) and elemental maps (b–e, g–j) of goethite particles embedded in resin. Images (a–e) correspond to a thin specimen ($t/\lambda = 0{\cdot}4$), and images (f–j) correspond to a thick specimen ($t/\lambda = 1{\cdot}3$). Images were acquired either on the Fe-$M_{2,3}$ (b,c,g,h) or on the Fe-$L_{2,3}$ (d,e,i,j) ionization edges. Elemental mapping was obtained either with the two-windows (JR; b,d,g,i) or with the three-windows (ESI; c,e,h,j) method.

Conclusion

Goethite particles embedded in resin and sectioned at different thicknesses satisfy the conditions for both model environmental particles and iron-rich EF-TEM standards. In the case of the Fe-$M_{2,3}$ absorption edge, it was possible to calculate a valid estimate of the partial cross-section $\sigma_{\text{Fe-M}_{2,3}}$ under our working conditions (80 keV). Because of the weakness of the background extrapolation in the low-loss region, the relative quantification of the Fe:O ratio is more suited to the Fe-$L_{2,3}$ absorption edge; this quantification generates errors lower than 20% in the 20–200 nm thickness range. For visualizing aims, however, the Fe-$M_{2,3}$ edge is a comfortable alternative to the use of the Fe-$L_{2,3}$ edge, especially for thick specimens.

Table 1. Signal-to-background ratios ($s/\sqrt{B}$) measured on the elemental maps of Fig. 6. For thin sections, signal and background are averages of 25 intensity measurements on individual pixels in the centres of the particles and around the particles. For thick sections, 550 randomly distributed pixels were measured on the particles and 50 pixels on the background.

$S/\sqrt{B}$	Fe-$M_{2,3}$ JR	Fe-$M_{2,3}$ ESI	Fe-$L_{2,3}$ JR	Fe-$L_{2,3}$ESI
$t/\lambda = 0{\cdot}4$	11	18	46	22
$t/\lambda = 1{\cdot}3$	22	12	29	13

Acknowledgments

Professor G. G. Leppard and D. Flannigan (McMaster University, Canada; ultramicrotomy), Dr D. Bazett-Jones (University of Calgary, Canada; access on EM) and Dr S. Fakan (Université de Lausanne, Switzerland; access on EM) are gratefully acknowledged. This work was supported by grants from the Swiss National Science Foundation (project 20-42250.94), the Agassiz Fund (Lausanne) and the Foundation of the 450th Anniversary (Lausanne).

References

Bachhuber, K. & Frösch, D. (1983) Melamine resins, a new class of water-soluble embedding media for electron microscopy. *J. Microsc.* **130,** 1–9.

Bennett, J.C., Cheng, S.C. & Egerton, R.F. (1994) The use of NiO test specimens in analytical electron microscopy. *ICEM 13, Paris*, 17–22 July, pp. 613–614.

Budd, P.M. & Goodhew, P.J. (1988) *Light-Element Analysis in the Transmission Electron Microscope; WEDX and EELS*. Oxford University Press, Oxford.

Buffle, J. (1988) *Complexation Reactions in Aquatic Systems: an Analytical Approach*. Ellis Horwood, Chichester.

Buffle, J. & Leppard, G.G. (1995a) Characterization of aquatic colloids and macromolecules. 1: Structure and behavior of colloidal material. *Environ. Sci. Technol.* **29,** 2169–2175.

Buffle, J. & Leppard, G.G. (1995b) Characterization of aquatic colloids and macromolecules. 2: Key role of physical structures on analytical results. *Environ. Sci. Technol.* **29,** 2176–2184.

Buffle, J. & van Leeuwen, H.P. (1992) *Environmental Particles*, Vol. 1. Lewis Publishers, Chelsea.

Buffle, J. & van Leeuwen, H.P. (1993) *Environmental Particles*, Vol. 2. Lewis Publishers, Chelsea.

Castaing, R. & Henry, L. (1962) Filtrage magnétique des vitesses en microscopie électronique. *C.R. Acad. Sci. Paris*, **B255,** 76–78.

Chandler, J.A. (1977) *X-Ray Microanalysis in the Electron Microscope*. North-Holland, Amsterdam.

Colliex, C. (1991) ELNES in the iron–oxygen system. *Phys. Rev. B,* **44,** 11402–11411.

Davison, W. & De Vitre, R. (1992) Iron particles in freshwater. *Environmental Particles*, Vol. 1 (ed. by J. Buffle and H.P. van Leeuwen), pp. 315–355. Lewis Publishers, Chelsea.

Degueldre, C., Longworth, G., Moulin, V. & Vilks, P. (1989) Grimsel colloid exercise; an international intercomparison exercise on

the sampling and characterisation of groundwater colloids. *PSI-report 39*. Paul Scherrer Institute, Würrenlingen.

Ditchfield, R.W. (1975) Measurement and interpretation of the EELS of iron and its oxides. *Solid State Commun.* **17,** 1367–1368.

Door, R., Frösch, D. & Martin, R. (1991) Estimation of section thickness and quantification of iron standards with EELS. *J. Microsc.* **162,** 15–22.

Eberhart, J.P. (1995) *Structural and Chemical Analysis of Materials*. John Wiley & Sons, Chichester.

Egerton, R.F. (1986) *Electron Energy-Loss Spectroscopy in the Electron Microscope*. Plenum Press, New York.

Egerton, R.F. & Cheng, S.C. (1994) Characterization of an analytical electron microscope with a NiO test specimen. *Ultramicroscopy,* **55,** 43–54.

Egerton, R.F. & Sevely, J. (1983) Jump-ratio as a measure of spectrometer performance. *J. Microsc.* **129,** RPI–RP2.

Hofer, F. & Wilhelm, P. (1993) EELS microanalysis of the elements Ca to Cu using $M_{2,3}$ edges. *Ultramicroscopy,* **49,** 189–197.

Hofer, F., Warbichler, P., Buchmayr, B. & Kleber, S. (1996) On the detection of MX-precipitates in micro-alloyed steels using energy-filtering TEM. *J. Microsc.* **184,** 163–174.

Johnson, D.E. (1979) Energy-loss spectrometry for biological research. *Introduction to Analytical Electron Microscopy.* (ed. by J.J. Hren, J.I. Goldstein and D.C. Joy), pp. 245–258. Plenum Press, New York.

Leppard, G.G. (1992a) Evaluation of electron microscope techniques for the description of aquatic colloids. *Environmental Particles,* Vol. 1. (ed. by J. Buffle and H.P. van Leeuwen), pp. 231–289. Lewis Publishers, Chelsea.

Leppard, G.G. (1992b) Size, morphology and composition of particulates in aquatic ecosystems: solving speciation problems by correlative electron microscopy. *Analyst,* **117,** 595–603.

Lienemann, C.-P., Mavrocordatos, D. & Perret, D. (1997) Enhanced visualization of polysaccharides from aqueous suspensions. *Mikrochim. Acta,* **126,** 123–129.

Mavrocordatos, D., Lienemann, C.-P. & Perret, D. (1994) Energy filtered transmission electron microscopy for the physico-chemical characterization of aquatic submicron colloids. *Mikrochim. Acta,* **117,** 39–47.

Mavrocordatos, D. & Perret, D. (1995) Non-artifacted specimen preparation for transmission electron microscopy of submicron soil particles. *Commun. Soil Sci. Plant Anal.* **26,** 2593–2602.

Nomizu, T. & Mizuike, A. (1986) Electron microscopy of submicron particles in natural waters; specimen preparation by centrifugation. *Mikrochim. Acta,* **I,** 65–72.

Perret, D., Lienemann, C.-P. & Mavrocordatos, D. (1995) EELS-ESI identification of heterogeneous suspensions of aquatic microparticles. *Microsc. Microanal. Microstruct.* **6,** 41–51.

Perret, D., Newman, M.E., Nègre, J.-C., Chen, Y. & Buffle, J. (1994) Submicron particles in the Rhine river. 1: Physico-chemical characterization. *Water Res.* **28,** 91–106.

Reed, S.J.B. (1993) *Electron Microprobe Analysis*. Cambridge University Press, Cambridge.

Robards, A.W. & Wilson, A.J. (1993) *Procedures in Electron Microscopy.* John Wiley & Sons, Chichester.

Salomons, W. & Förstner, U. (1984) *Metals in the Hydrocycle*. Springer-Verlag, Berlin.

Schwertmann, U. & Cornell, R.M. (1991) *Iron Oxides in the Laboratory.* VCH Verlag, Weinheim.

Sigg, L. (1985) Metal transfer mechanisms in lakes; the role of settling particles. *Chemical Processes in Lakes*, (ed. by W. Stumm), pp. 283–310. Wiley-Interscience, New York.

Sigg, L. (1987) Surface chemical aspects of the distribution and fate of metal ions in lakes. *Aquatic Surface Chemistry* (ed. by W. Stumm), pp. 319–349. Wiley-Interscience, New York.

Zaluzec, N.J. (1983) The influence of specimen thickness in quantitative energy-loss spectroscopy. *41st Ann. Proc. Electron Microsc. Soc. Am*. pp. 388–389. San Francisco Press, San Francisco.